Photoaquation Mechanism of Hexacyanoferrate(II) ions: Ultrafast 2D UV and Transient Visible and IR Spectroscopies

Marco Reinhard[1†], Gerald Auböck[1‡], Nicholas A. Besley[2], Ian P. Clark[3], Gregory M. Greetham[3], Magnus W. D. Hanson-Heine[2], Raphael Horvath[2], Thomas S. Murphy[2], Thomas J. Penfold[4], Michael Towrie[3], Michael W. George[2,5] and Majed Chergui[1]

[1]Ecole polytechnique Fédérale de Lausanne, Laboratoire de spectroscopie ultrarapide, ISIC and Lausanne Centre for Ultrafast Science (LACUS), FSB, Station 6, CH-1015 Lausanne, Switzerland

[2]School of Chemistry, University of Nottingham, Nottingham NG7 2RD, United Kingdom

[3]Central Laser Facility, Research Complex at Harwell Science and Technology Facilities Council, Rutherford Appleton Laboratory, Harwell Oxford, Didcot, Oxfordshire OX11 0QX, United Kingdom

[4]School of Chemistry, Newcastle University, Newcastle upon Tyne NE1 7RU, United Kingdom

[5]Department of Chemical and Environmental Engineering, University of Nottingham Ningbo China, 199 Taikang East Road, Ningbo 315100, China

Mike.George@nottingham.ac.uk; majed.chergui@epfl.ch

[†] Now at : PULSE Institute for Ultrafast Energy Science, Stanford, USA

[‡] Now at : CTR Carinthian Tech Research AG; Europastrasse 4/1, 9524 Villach/St. Magdalen, Austria.

Abstract

Ferrous iron(II) hexacyanide in aqueous solutions is known to undergo photoionization and photoaquation reactions depending on the excitation wavelength. In order to investigate this wavelength dependence, we implemented ultrafast two-dimensional UV transient absorption spectroscopy, covering a range from 280 to 370 nm in both excitation and probing, along with UV pump/visible or IR continuum probe transient absorption spectroscopy and density functional theory (DFT) calculations. As far as photoaquation is concerned, we find that excitation of the molecule leads to ultrafast intramolecular relaxation to the lowest triplet state of the $[Fe(CN)_6]^{4-}$ complex, followed by its dissociation into CN^- and $[Fe(CN)_5]^{3-}$ fragments and partial geminate recombination, all within <0.5 ps. The subsequent time evolution is associated with the $[Fe(CN)_5]^{3-}$ fragment going from a triplet square pyramidal geometry, to the lowest triplet trigonal bipyramidal state in 3-4 ps. This is the precursor to aquation, which occurs in ~20 ps in H_2O and D_2O solutions, forming the $[Fe(CN)_5(H_2O/D_2O)]^{3-}$ species, although some aquation also occurs during the 3-4 ps time scale. The aquated complex is observed to be stable on the microsecond timescale. For excitation below 310 nm, the dominant channel is photooxidation with a minor aquation channel. The photoaquation reaction shows no excitation wavelength dependence up to 310 nm, i.e. it reflects a Kasha Rule behaviour. In contrast, the photooxidation yield increases with decreasing excitation wavelength. The data from 2DUV, transient visible absorption and time resolved infrared (TRIR) absorption experiments are fully consistent. The various intermediates that appear in the TRIR studies are identified with the help of DFT calculations. These results provide a clear example of the energy dependence of various reactive pathways and of the role of spin-states in the reactivity of metal complexes.

Introduction

Most of natural and preparative (bio)chemistry occurs in the liquid phase. The solvent molecules are by no means spectators as they may affect the outcome of the reactions in different ways, either dynamically by influencing the course of the reaction, e.g. hindering it as in the so-called cage effect,[1] or by accelerating it, offering a driving force to the escape of products into the solvents;[2,3] and/or statically by introducing relative energy shifts of the reactive potential surfaces on which the reactions (including photochemical ones) occur, according to the nature (covalent, charge transfer or, even Rydberg) of the states involved.[4] For many years now, since the historical paper by Frank and Rabinowitsch,[1] the physical effects of the solvent cage on photochemical reactions have intensely been studied by steady-state,[4-6] and time-resolved methods[2,3,6-8] on a wide class of systems. Less studied are the chemical pathways of the solution phase where intermediates react with solvent species, as discussed in a recent review.[3] The complexity of such processes arises from the fact that either the excited solute or a nascent product sees a complex potential surface in its interaction with solvent molecules, which no longer just provide a barrier or a funnel to it, but participate in the chemical reaction depending on several aspects such as the nature of the reactants, their translational kinetic energy, their internal (electronic, vibrational, rotational) energy, their orientation, etc.

In attempting to describe liquid phase photochemistry, fundamental questions arise, which concern: a) the role of the initially excited state, b) the interplay between intramolecular relaxation (electronic or vibrational) in the solute/intermediates and the subsequent reactivity with solvent molecules; c) the role of spin states of both educts and products; d) the role of the excess energy dependence of the photochemical reactions. While a larger excess of kinetic energy of the fragments allows overcoming "physical" solvent cage barriers,[5,9] the question remains open for the case of chemical reactions.

In addressing these questions, ligand substitution reactions and redox decomposition processes of metal complexes have been the topic of several mechanistic studies in coordination chemistry because of the fundamental role such reactions play in various chemical, biological and catalytic

processes.[10,11] In such systems, ultrafast intramolecular energy relaxation processes, such as internal conversion (IC), intersystem crossings (ISC) and intramolecular vibrational energy redistribution (IVR) in the solute may precede the reaction or be concurrent to it. These processes may also occur in the products if these are formed in excited states. In addition, intermolecular processes such as solvation dynamics, may take place concurrently with the above intramolecular ones,[2] and the spin multiplicity plays a crucial role in the reactions leading to ligand substitution.[12]

Metal carbonyls have been among the most studied systems, probably because they offer the possibility to compare the photochemistry of the isolated molecule with that in condensed phases. Studies of the latter include UV photolysis in low temperature inert matrices,[13] and several ultrafast spectroscopic studies in solution using transient absorption (TA) in the visible,[14-19] and in the infrared.[20-24] More recently, ultrafast studies on the photochemistry of $Fe(CO)_5$ in solution have been pushed into the x-ray domain and an Fe K-edge x-ray absorption study was reported by Rose-Petruck and co-workers,[25] while Wernet *et al.*[26,27] implemented femtosecond Fe L_3-edge resonant inelastic x-ray scattering (RIXS) at the x-ray Free Electron Laser in Stanford. RIXS, which is a variant of x-ray emission spectroscopy, is a sensitive probe of the spin state of molecular systems. The studies on the photo-induced dynamics of $Fe(CO)_5$ in EtOH suggest formation of the $^1[Fe(CO)_4(EtOH)]$ complex, and the role of the spin state of the $Fe(CO)_4$ product is still debated. Wernet *et al*.[26] reported a singlet complexation on sub-picosecond time scales, which was ascribed to a barrier-less bimolecular reaction where steric effects such as ethanol reorientation and concomitant hydrogen-bond breaking are absent or can easily be overcome.[27] This fast photosubstitution is in line with reports of CO-ligand substitution of $[Cr(CO)_4(bpy)]$ by solvent molecules,[28-32] from a vibrationally "hot" excited state, alongside relaxation into two lower-lying unreactive states. In this case, dependence on excess energy was observed as the quantum yield of the reaction increased with excitation energy. It was argued that vibrational excitation provides sufficient distortion of the reacting molecule in the direction of the transition state whose structure was described as being similar to the undissociated excited molecule.

Photoaquation is a particular case of the broader class of ligand substitution reactions in solutions and its understanding is particularly relevant to biology.[33] It was recently studied in the case of *cis*-$[Ru(bpy)_2(CH_3CN)_2]Cl_2$ in water, showing the stepwise replacement of each CH_3CN ligand by an H_2O molecule,[34] with the formation of the monoaqua *cis*-$[Ru(bpy)_2(CH_3CN)(H_2O)]^{2+}$ taking place in <100 ps. One of the earliest examples of studies on photoaquation concerns metal cyanide systems[35-38], such as $[Fe^{II}(CN)_6]^{4-}$, whose absorption spectrum is shown in Figure 1. The peculiarity of this system stems from the fact that it is a highly charged ion that has a strong interaction with the solvent.[39-41] Both oxidation (Equation 1) and aquation (Equation 2) processes have been reported upon irradiation in the UV-visible range[42,43]:

$$[Fe(CN)_6]^{4-*} \rightarrow [Fe(CN)_6]^{3-} + e^-_{aq} \quad (1)$$

$$[Fe(CN)_6]^{4-*} + H_2O \rightarrow [Fe(CN)_5(H_2O)]^{3-} + CN^- \quad (2)$$

With the advent of ultrafast laser techniques, detailed femto- and picosecond TA studies of the photooxidation reaction (Equation 1) have been performed.[44-47] It is generally believed this reaction is a consequence of direct or indirect population of the Charge-Transfer-to-Solvent (CTTS) state (Figure 1).[42] A tentative assignment of the very short-lived (<< 60 fs) CTTS-state, absorbing around 490 nm upon 267 nm excitation was made by ultrafast transient absorption (TA),[45] but it was assumed that the initially populated $^1T_{2g}$-state relaxes into the CTTS state and therefore, the authors could not unambiguously distinguish between these two states. Ultrafast fluorescence up-conversion indeed failed to detect the CTTS state of $[Fe(CN)_6]^{4-}$,[48] contrary to the case of aqueous iodide.[49]

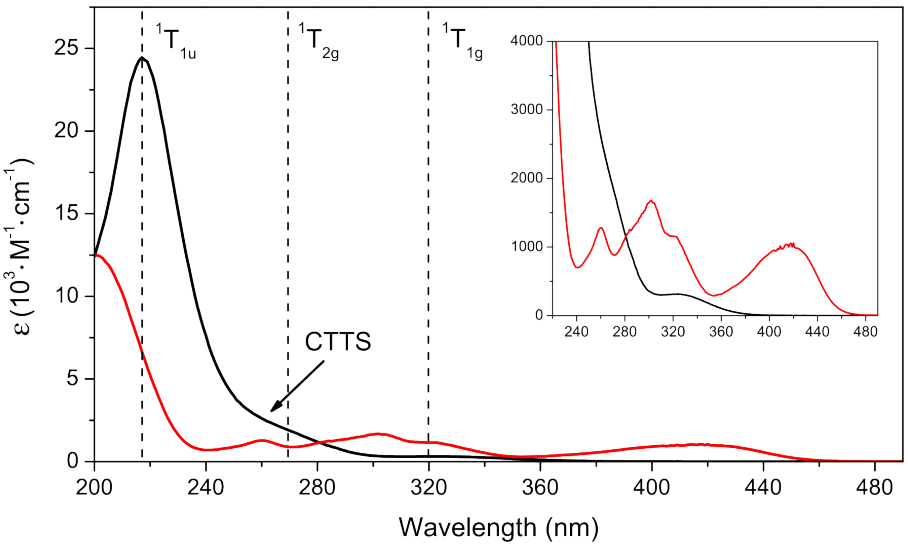

Figure 1. Extinction coefficients of solvated $[Fe(CN)_6]^{4-}$ (black line) and $[Fe(CN)_6]^{3-}$ (red line) in water. The vertical dashed lines show the energies of relevant excited states of $[Fe(CN)_6]^{4-}$ in water. The inset shows magnified spectra, highlighting the lower-intensity transitions.

Anderson *et al*.[46] investigated the ionization process upon 266 nm excitation using time-resolved infrared (TRIR) spectroscopy. Their transient spectra in the ν(CN) region in D_2O, show a significant baseline offset, which they attributed to a direct precursor of the pre-solvated electron generated by excitation of the CTTS state. Furthermore, they observed a short-lived absorption peak red-shifted by ca. 2 cm^{-1} from the parent ion (at 2038 cm^{-1}) as well as a band at 2114 cm^{-1} due to the photoionized product $[Fe(CN)_6]^{3-}$. The appearance of the latter at the earliest time delays indicates electron-ejection in less than 200 fs.[46]

The reaction shown in Equation 2 is less well understood. It is triggered by excitation of weak Laporte-forbidden ligand-field (LF or metal-centered) states ($\varepsilon \lesssim 400$ $M^{-1}\cdot cm^{-1}$) for $\lambda > 300$ nm[50] or, with a lower yield, in the ~245 - 300 nm range, where the CTTS and LF bands overlap (Figure 1). Using flash photolysis, Shirom and Stein[43] identified the photoaquated species via an absorption band in the 380-480 nm region which they attributed to the $^1A_1 \rightarrow {}^1E(1)$[51] transition of the $[Fe(CN)_5(H_2O)]^{3-}$

complex, and concluded that it is formed within one nanosecond. Quantum yields for aquation (ϕ_{aq}) were found to depend on the excitation wavelength, pH and on concentration[35,52] and the extracted values have large uncertainties. In 10 mM neutral solutions, $\phi_{aq} \sim 0.2$ was reported for 313 nm and 365 nm excitation and ~0.1 for 254 nm excitation, indicating that an increasing energy decreases ϕ_{aq} and pointing to another competing relaxation channel at higher energies,[42] which is most likely the photooxidation channel.

Recently, Reinhard *et al.* reported a x-ray absorption spectroscopy study with 70 ps time resolution of aqueous ferric and ferrous hexacyanide upon 355 nm and 266 nm excitation, combined with quantum chemical calculations.[48] In the case of the ferrous complex upon 355 nm excitation, they identified the aquated $[Fe(CN)_5(H_2O)]^{3-}$ species, confirming the conclusions of optical studies,[43] and they determined its molecular structure. Upon 266 nm excitation, the main photoproduct was the ferric hexacyanide complex. The limited time resolution of their experiment did not allow for the time scale of photoaquation and therefore, its mechanism to be determined.

It is indeed unclear if photoaquation of $[Fe(CN)_6]^{4-}$ starts by dissociation of a CN-ligand followed by binding of a solvent molecule or if the process is concerted. In either case, the next question is whether dissociation starts from the lowest lying singlet $^1T_{1g}$ state or the system undergoes fast ISC to the $^3T_{1g}$ or even the $^5T_{2g}$ state, which was theoretically predicted[53] but never identified. By measuring small but positive activation volumes of the ferrocyanide photoaquation reaction, Finston and Drickamer[54] excluded a purely associative mechanism, which would involve an intermediate with bond formation between the complex and the solvent molecule. They argued that photoaquation is likely to proceed via a dissociative interchange pathway in which ligand-to-metal bond breaking and solvent-to-metal bond formation are concerted. This seems consistent with density functional theory (DFT) calculations,[53] which estimated the ground state dissociation energy to 6.2 eV per Fe-CN bond, while photoaquation already occurs for 3.4 eV excitation into the $^1T_{1g}$ state. However, these calculations concern the isolated molecule, excluding solvent effects, which may strongly affect the energetics of the system. Indeed, an association mechanism may be compatible with recent x-ray[39,41] and IR[40,55]

studies, hinting to a specific interaction between the solute and water molecules in the ground state of the complex.

The occurrence of excitation energy dependent reaction channels (oxidation, aquation) in the photochemistry of $[Fe(CN)_6]^{4-}$ and the fact that it is a highly charged educt make it an ideal system for the description of solution phase ultrafast chemical dynamics. We recently demonstrated the power of ultrafast 2-dimensional (2D) ultraviolet (UV) transient absorption (TA) spectroscopy,[56-58] to disentangle concurrent excitation energy–dependent relaxation channels in biological and chemical systems. Here, we combine it with ultrafast UV pump/visible continuum probe and UV pump/IR continuum probe[59] TA spectroscopy to disentangle the excitation wavelength dependence of the processes described by Equations 1 and 2 in aqueous $[Fe(CN)_6]^{4-}$.[42,43] The present combination of techniques allows an unambiguous assignment of the photoproducts and of their time scales of formation for excitation wavelengths below and above 310 nm in H_2O and D_2O covering the time range from <1 ps to 100 μs. Finally, DFT calculations have been carried out to simulate the geometries and vibrational frequencies of $[Fe(CN)_6]^{4-}$ and of some of its predicted photoproducts, both *in vacuo* and in solution. The results suggest that following photoexcitation, the system relaxes to the lowest triplet state from which dissociation occurs, leading to the formation of a triplet $[Fe(CN)_5]^{3-}$ complex. The latter undergoes conformational changes prior to binding of a water molecule. Further details about the experimental and computational set-ups and procedures as well as the data treatment are given in the supporting information (SI).

Experimental

Time-resolved Infrared (TRIR) spectroscopy

TRIR spectroscopy was carried out using the ULTRA facility located at the Rutherford Appleton Laboratory, using time resolved multiple probe spectroscopy (TR^MPS) on the ULTRA and LIFEtime instruments. Detailed descriptions of the experimental setups have been published previously.[59,60]

Briefly, the TR^{M}PS experiment utilizes a pump-probe-probe-probe… recording scheme afforded by synchronizing two oscillators with the pump laser tuned to 320 or 266 nm by optical parametric amplification (OPA) while the mid-IR probe is generated using OPAs with difference-frequency mixing units. The pump-probe time delay is controlled using a combination of electronic and optical delays, which allows time-delays from ps to ms to be achieved in a single experiment. The instrument response ($\tau_{IRF,IR}$) is approximately 300 to 400 fs. The pump pulse was set to *ca.* 1 μJ/pulse at the sample using a neutral density filter. Pump and probe beam polarizations were set at the magic angle. Where necessary a portion of the probe beam was dispersed onto an MCT detector as a reference, while the remainder was passed through the sample, dispersed by grating monochromators and detected by 128-channel linear MCT array detectors. $[Fe(CN)_6]^{4-}$ samples were measured in unbuffered H_2O and D_2O (18 mM) and were circulated in a closed flow system attached to a Harrick solution cell with CaF_2 windows, spaced by 100 μm with Teflon spacers. The sample cells were rastered in the two dimensions orthogonal to the direction of beam propagation in order to minimize sample breakdown and localized heating. The spectral resolution is *ca.* 1.5 cm^{-1}.

Two-dimensional Ultraviolet (2D-UV) spectroscopy:

A detailed description of the set-up was recently published.[56-58] Laser pulses from a cryogenically cooled Ti:Sapphire amplifier (Wyvern, KM Labs) running at 20 kHz, pump a non-collinear optical parametric amplifier (NOPA, TOPAS white, Light Conversion) whose output serves as primary light source of the experiment. One third of the generated visible light passes a motorized delay line and subsequently an achromatic frequency doubling stage, which delivers broad band UV probe pulses in the 270 - 360 nm range. After the sample, probe pulses are dispersed by a fiber coupled spectrograph and detected on a shot-to-shot basis with a CMOS linear image array. The remaining two thirds of the NOPA output are directed through a chopper which is phase-locked to half the repetition rate of the laser system (10 kHz) and passes a motorized BBO-crystal whose angle is adjustable with respect to

the incident beam in order to allow for a frequency tunable narrow-band pump beam without significantly changing the spatial overlap with the probe beam. Polarizations of pump and probe beams were parallel and at all pump wavelengths used, fluences were 0.6 mJ/cm^2.

Samples of 30 mM $[Fe(CN)_6]^{4-}$ in unbuffered aqueous solution (deionized H_2O) were prepared from purchased potassium ferrocyanide ($K_4Fe(CN)_6 \cdot 3H_2O$, Sigma Aldrich) and measured in a 100 μm liquid jet. Pure solvent scans did not yield any signals apart from cross-phase modulation (CPM), whose width we use to estimate the instrumental response function of $\tau_{IRF,UV} \approx$ 150 fs. However the relatively small sample signals may be distorted up to ca. 300 fs and we refrain from interpreting data at shorter delays.

UV-pump/visible-probe experiments

To complement the 2D UV transient absorption studies, we also carried out UV pump/visible probe measurements of aqueous $[Fe(CN)_6]^{4-}$ with a white light continuum probe in the 380 - 480 nm region generated from a small portion of the 800 nm fundamental. The TOPAS white output and motorized BBO-crystal rotation were optimized for efficient pumping at 323 nm with ca. 1.3 mJ/cm^2. The number of detector counts is significantly lower in the visible probe region and due to noise limitations in this case, we used a 500 µm flow cell instead of the thinner liquid jet used in the 2D UV experiment. The larger thickness was chosen in order to minimize the accumulation of photoproducts at the cell windows. In addition, during the measurements, the cell was regularly moved within the spatial pump-probe overlap region, ensuring the integrity of the accumulated signal scans during the measurements. In order to maintain an optical density of ~ 0.3 a sample concentration of 0.02 M was chosen. The relatively large sample thickness increases the instrument response function from ~ 150 fs

in the UV-probe experiments to $\tau_{IRF,visible} \sim 690$ fs in the visible-probe experiments as determined from the cross-phase modulation (CPM) on pure water solutions. Further support for this decrease in time-resolution at earlier times stems from measurements of PPO in cyclohexane where we measured a comparable $\tau_{IRF,visible}$ even though the signal rise time is known to be much faster than 150 fs. Pump and probe polarizations were at magic angle.

Results

The photochemistry $[Fe(CN)_6]^{4-}$ in aqueous solutions had previously been reported[42,43] for only a few fixed excitation wavelengths. In addition, the ultrafast visible[45] and IR[46] studies carried out so far only considered excitation into the CTTS states of $[Fe(CN)_6]^{4-}$ at 266 nm (Figure 1 and Equation 1). Here we complement these studies by covering the excitation range from 280 to 330 nm, using two-dimensional UV transient absorption spectroscopy in H_2O and we focus on specific excitation wavelengths using ~~ps~~-TRIR in H_2O and D_2O. Given the scarcity of ultrafast studies, it is important to benchmark our TRIR experiments against those previously reported under 266 nm excitation.[46]

TRIR spectra of $[Fe(CN)_6]^{4-}$ in H_2O and D_2O, at fixed time delays following excitation at a pump wavelength (λ_{pump}) of 266 nm are shown in Figures S1 and S2. There is a significant baseline offset at early times. These results are in agreement with previous studies that assigned the change in the mid-IR baseline to the precursor of the pre-solvated electron.[46] The parent band (2038 cm^{-1}) is bleached and a new transient peak at 2117 cm^{-1} is visible within ~1 ps, with the earlier times obscured by the baseline offset mentioned above. The band at 2117 cm^{-1} is due to formation of the ferricyanide ion, $[Fe(CN)_6]^{3-}$, consistent with ref. [46]. The kinetic traces of significant bands for the sample in H_2O are shown in Figure S3 and are similar in the case of D_2O. There is a partial recovery of the parent with a concomitant partial decrease of the intensity of the 2117 cm^{-1} band observed on the nanosecond timescale, fully consistent with the partial recombination of the solvated electron with $[Fe(CN)_6]^{3-}$.[47] The $[Fe(CN)_6]^{3-}$ band then persists up to the longest time delays in our experiment (Figure S2). At early times (Figure

S3(a)), an apparent partial recovery of the parent bleach band at 2038 cm^{-1} occurs on a time scale of τ = 20 ± 5 ps. The band frequencies and their timescales are summarised in Table 1. A band is also observed at ~2088 cm^{-1} at early times, whose decay seems to be independent to the $[Fe(CN)_6]^{3-}$ band at 2117 cm^{-1}. We discuss it further below. In order to disentangle contributions from different photochemical channels we now turn to 2D UV TA spectroscopy.

Figure 2 shows the 2D UV TA spectra (ΔA) of aqueous $[Fe(CN)_6]^{4-}$ as a function of pump (λ_{pump}) and probe (λ_{probe}) wavelengths at selected delays (Δt = 0.5, 1, 4 and 50 ps). After 50 ps, there is only little change in the observed transient signals, which remain stable up to the limit of our temporal window (~780 ps). Two main trends characterize the time and spectral evolution of the system as a function of λ_{pump}: one below ~310 nm, and the other above. There is a clear dependence of the appearance of spectral features on λ_{pump} and upon excitation into the CTTS region (*ca.* 290 nm), the transient ground state $[Fe(CN)_6]^{3-}$ absorption bands can be identified, resulting from photooxidation (dashed red line in 50 ps window). The $[Fe(CN)_6]^{3-}$ band is formed within our time resolution (~150 fs) and partially decays due recombination with the photoejected electrons.

At lower energy, in the region of the $^1T_{1g}$ absorption (blue line in Figure 2), a < 1 ps-lived positive signal appears, which is most pronounced in the highest-energy part of the probe range (< 280 nm). At λ_{probe} < 340 nm, this signal decays and becomes negative such that by ~50 ps, it resembles the inverted static $[Fe(CN)_6]^{4-}$ absorption spectrum (Figure 2, 50 ps window, red line), reflecting a long-lived ground state bleach. At λ_{probe} > 340 nm, the signal remains positive, indicating a long-lived absorption band. Therefore, direct excitation of the $^1T_{1g}$ state yields long-lived species, which is (are) not explained in terms of a photooxidized product, $[Fe(CN)_6]^{3-}$. In the following, we will mainly focus on results obtained at λ_{pump} = 284 nm and λ_{probe} = 320 nm, which are representative of the processes described by Equations 1 and 2 above.

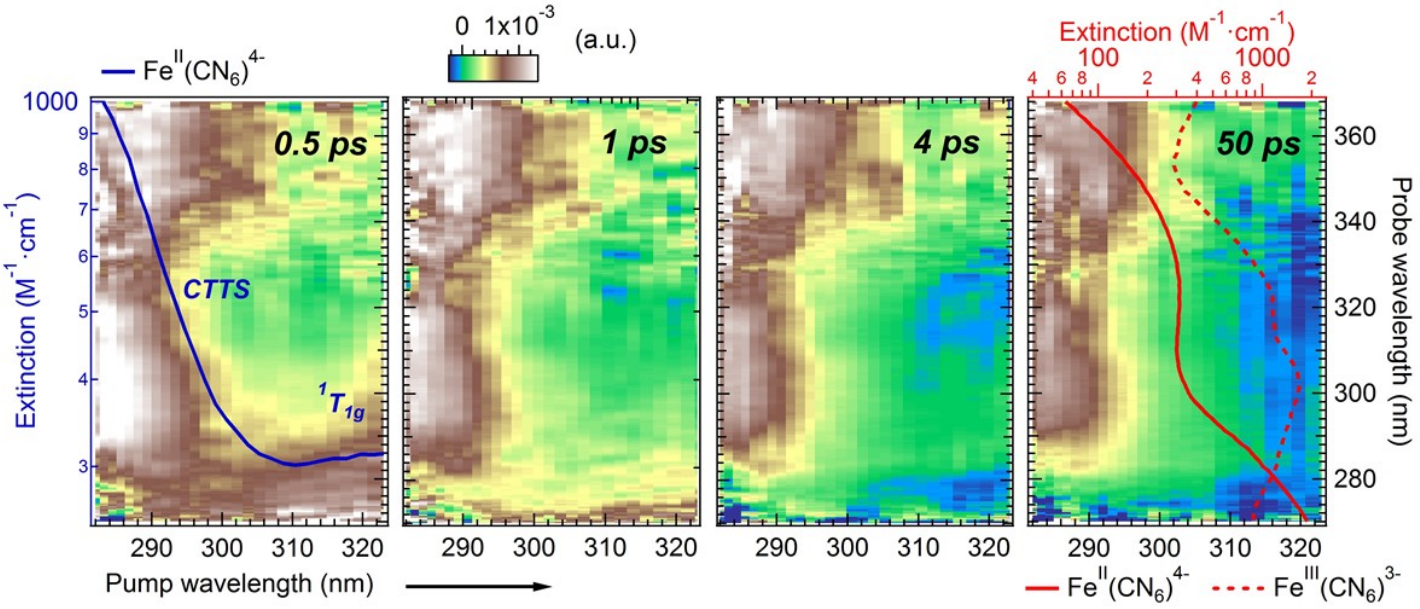

Figure 2. Pump intensity corrected 2D spectra of aqueous $[Fe(CN)_6]^{4-}$ as a function of pump (horizontal axis) and probe (vertical left axis) wavelength. The extinction coefficient (in $M^{-1}\cdot cm^{-1}$) of $[Fe(CN)_6]^{4-}$ vs. pump wavelength is represented by the blue line (left vertical axis) in the leftmost panel and vs. probe wavelength by the solid red line (horizontal upper axis) in the rightmost panel. The extinction coefficient of $[Fe(CN)_6]^{3-}$ is shown by the dashed red line. CTTS and $^1T_{1g}$ regions of the $[Fe(CN)_6]^{4-}$ extinction coefficient are indicated.

As discussed before, previous time-resolved optical and x-ray studies,[42,43,46,48] showed that photoaquation is the favored process after $^1T_{1g}$ excitation (320 nm), while the signal upon <300 nm excitation is predominantly due to photooxidation. Figures 3(a) and (c) compare the transient spectra at 284 nm and 320 nm excitation, at different integrated pump-probe delay windows. Relatively large temporal integration ranges are chosen for enhanced clarity but all conclusions are confirmed by averages over smaller ranges (Figures S4 and S5). Both figures show a dominant absorption in the blue most part (<300 nm) of the probe range, which quickly disappears (within 1-2 ps), leaving the transient with a profile that does not evolve much thereafter. In Figure 3(a), the transients at later times are dominated by the broad absorption of the $^2T_{2g} \rightarrow {}^2T_{2u}$ ($t_{2u}\pi \rightarrow t_{2g}\pi$) ligand to metal charge transfer

(LMCT) band of $[Fe(CN)_6]^{3-}$ and the solvated electron (as demonstrated below).[47] In Figure 3(c), the transients show weak negative (bleach) and positive signals, which we discuss hereafter.

The solvated electron is characterized by an extinction coefficient that is much larger than that of all other photoproducts as can be seen in Figure S6. This induces a significant offset of the signals at all time delays. In order to identify the spectral features in Figures 3(a) and (c), the extinction coefficients (ε) of the expected photoproducts were used to simulate the final transient spectra. For the transient obtained by 284 nm excitation, the extinction coefficient is calculated as $\varepsilon_{284\,\mathrm{nm}} = 8 \cdot 10^{-7} \cdot (\varepsilon_{[Fe(CN)_6]^{3-}} + \varepsilon_{e^-_{aq}} - \varepsilon_{[Fe(CN)_6]^{4-}})$. The coefficients $\varepsilon_{[Fe(CN)_6]^{3-}}$, $\varepsilon_{[Fe(CN)_6]^{4-}}$ and $\varepsilon_{e^-_{aq}}$ are already known[61] (Figure S6). The resulting $\varepsilon_{284\,\mathrm{nm}}$ is shown as a black dashed line in Figure 3(a) and it overall agrees with the transient spectrum at the longest time delays (purple trace) despite some deviations between 295 and 330 nm.

In the case of 320 nm excitation, the most likely final product is the aquated species. We therefore calculate $\varepsilon_{320\,\mathrm{nm}} = 8 \cdot 10^{-7} \cdot (\varepsilon_{[Fe(CN)_5(H_2O)]^{3-}} - \varepsilon_{[Fe(CN)_6]^{4-}})$, where the value of $\varepsilon_{[Fe(CN)_6(H_2O)]^{3-}}$ is taken from literature.[62,63] The result is shown as a black dashed line in Figure 3(c) and it nicely reproduces the shape of the longest time delay transient, confirming the presence of the photoaquated species $[Fe(CN)_5(H_2O)]^{3-}$. The rising signal in the low energy part of the spectrum therefore likely reflects the tail of the $^1A_1 \rightarrow {}^1E(1)$ absorption band of $[Fe(CN)_5(H_2O)]^{3-}$, which is centered around 440 nm in the static absorption spectrum.

This is confirmed by probing at lower energies, in the 380 – 480 nm region, and Figure 4(a) shows the TA spectra in this region, averaged over different temporal windows. Indeed, absorption features appear within ~ 0.7 ps with maxima at ~ 400 nm and > 470 nm. After a fast initial decay, further evolution of the transient occurs with minor changes around 410 nm. At times > 15 ps, the TA spectrum (dark blue and purple traces) converges to the static difference spectrum of the $[Fe(CN)_5(H_2O)]^{3-}$ $^1A_1 \rightarrow {}^1E(1)$ transition) and $[Fe(CN)_6]^{4-}$ absorption ($\varepsilon_{320\,\mathrm{nm}}$, black dashed trace).

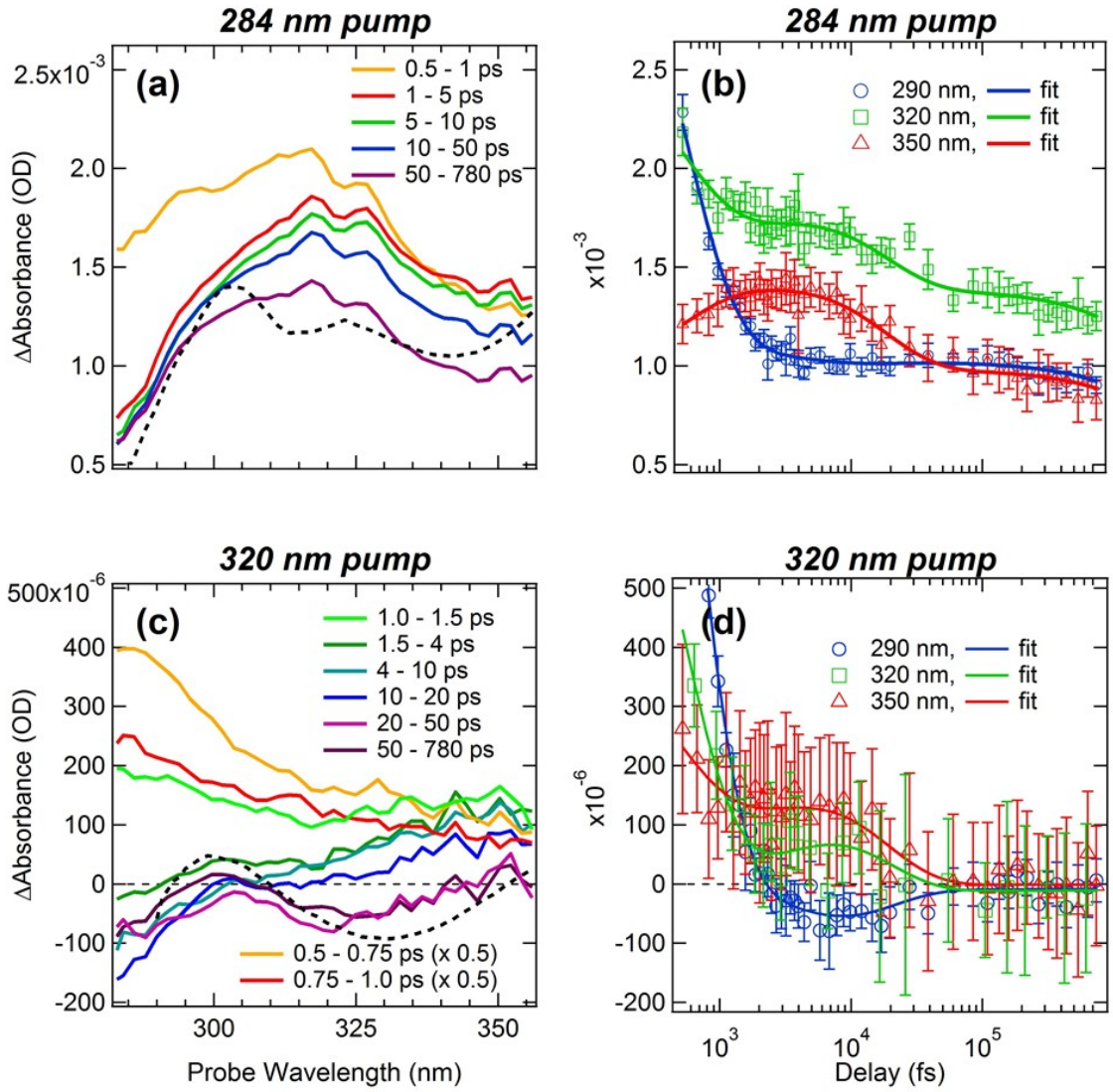

Figure 3. Averaged transient spectra and kinetic traces of aqueous $[Fe(CN)_6]^{4-}$ excited at (a,b) 284 nm and (c,d) 320 nm. The dashed black line in (a) corresponds to ε_{284nm} and the dashed line in (c) corresponds to ε_{320} nm, as defined in the text. Kinetic traces and fits with timescales (Table 1) derived from the full 3-dimensional dataset are shown in (b) and (d).

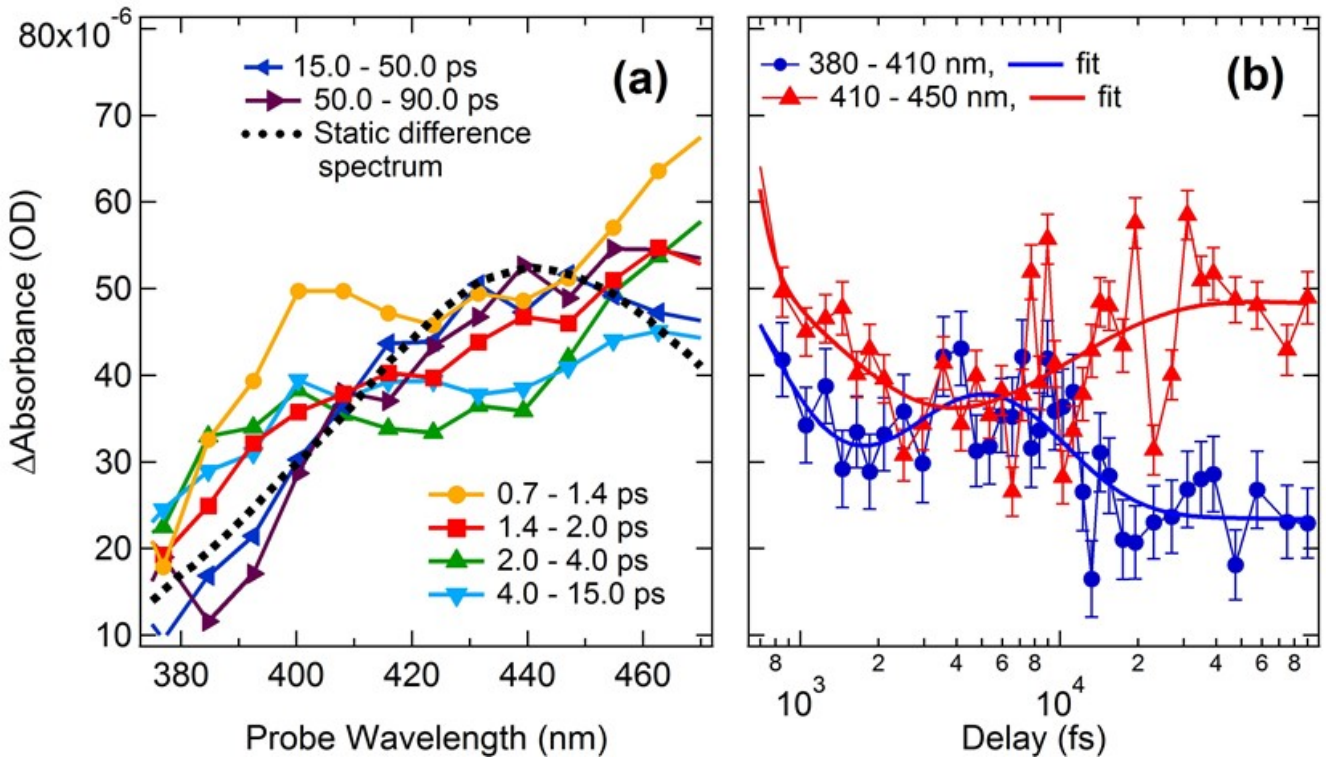

Figure 4. Visible probe transients following 323 nm excitation of aqueous $[Fe(CN)_6]^{4-}$. (a) Averaged spectra in the vicinity of the $^1A_1 \rightarrow {}^1E(1)$ absorption band of the aquated species. The dashed black line is the modelled static absorption difference of the $[Fe(CN)_5(H_2O)]^{3-}$ and $[Fe(CN)_6]^{4-}$ species ($0.1 \cdot \varepsilon_{320}$, see Figure 3) (b) Smoothed kinetic traces and fits with fixed timescales derived from the UV dataset (Table 1).

In order to gain a quantitative understanding of the 2D UV data, a global fit (GF) was carried out. Four exponential timescales are required in the photoaquation regime (320 nm excitation, see below). For both 284 nm and 320 nm excitation, transient spectra at delays around ~ 50 ps still display small changes (Figures 3, S4 and S5), presumably due to slow, non-exponential recombination kinetics of the corresponding photochemical species, these changes are not properly captured by our multiexponential kinetic model. Therefore, the inclusion of an additional timescale is avoided in favor of a more stable fit model. This strategy and the extracted time constants are fully confirmed by the IR results presented below. Fitting the initial decay requires two exponential timescales (τ_1 = 0.5 ps, τ_2 = 4

ps).[§] An additional time constant of ~16 ps (τ_3) is needed to capture the intermediate times. Representative kinetic traces for 284 nm and 320 nm excitation are shown in Figures 3(b) and 3(d) together with their fits. The time constant for the longest process obtained from the GF of the 2D UV dataset is $\tau_4 \sim 7$ ns (τ_4) but this value should be taken only as an order of magnitude, due to the limited range of the data set. The fitted time constants are summarized in Table 1.

To disentangle the spectral components making up the full 2D UV data set, we also applied a singular value decomposition (SVD) as described in refs [58,64] and in § S4. The SVD analysis of the 2D UV data set yields 2D Decay Associated Dispersed Action Spectra (DADAS)[58] associated with the four decay constants ($\tau_1 = 0.5 \pm 0.1$ ps, $\tau_2 = 4 \pm 2$ ps, $\tau_3 = 16 \pm 3$ ps, $\tau_4 \sim 7$ ns). All spectra are subsequently corrected for the photolysis yield (§ S2) in order to obtain signal magnitudes, which are directly comparable with quantum yields. The extracted four DADAS are plotted in Figure S7 and their detailed description is given in § S4.2. The consistency of the extracted parameters is confirmed by a fit of the kinetic traces integrated over the spectral regions 380 – 410 nm and 410 – 470 nm. The choice of these regions is justified by the spectral evolution shown in Figure 4(a). Assuming that the above four timescales of the UV-probe experiment also occur in the visible-probe region, we obtain a satisfactory fit of the kinetics, notwithstanding the poor signal-to-noise ratio (Figure 4(b)). Since the visible probe measurements were limited by an IRF of $\tau_{IRF,visible} \sim 690$ fs (see experimental section), we left out the fastest component in this analysis. The ~7 ns component appears in the analysis of both the 284 nm and the 320 nm excitation data. As already mentioned, this timescale is much longer than the time range of the measurements and is therefore, only indicative of slow processes that reflect the long-lived species upon 320 nm excitation and/or the electron-ferricyanide recombination upon 284 nm excitation.

With these elements in hand, we then extract the DAS in the combined UV-visible probe range for 320 nm excitation, which are shown in Figure 5(b), while Figure 5(a) shows the steady state spectra of $[Fe(CN)_6]^{4-}$ and of the aquated form. The 0.5 ps (τ_1) DAS is only constructed for the UV range due to the limited time resolution in the visible range, and it essentially shows the fast decay of the induced

[§] A stretched exponential fit was attempted but it poorly reproduced the data.

absorption peaking below 280 nm. In the visible range, an absorption band centered at λ_{probe} ~ 460 nm also appears within the time resolution of the experiment (see Figure 4(a)). The 4 ps (τ_2) DAS reflects a second, slower decay component of the induced UV (<320 nm) absorption and some spectral intensity redistribution from 410-480 nm to 380-410 nm of the absorption in the visible range. The 16 ps (τ_3) DAS displays a ground state bleach recovery below 320 nm and it mirrors the 4 ps DAS above 330 nm, pointing to an intensity redistribution back from 380-410 nm to 410-480 nm. The prominent negative feature of the 16 ps DAS in the 410-480 nm region reflects the rise of the ~7 ns (τ_4) DAS that has a broad and intense absorption covering the 380-480 nm range. The ~7 ns DAS is nicely reproduced by $\varepsilon_{320\,nm}$ (see above), and it can therefore be assigned predominantly to the $[Fe(CN)_5(H_2O)]^{3-}$ complex. As seen from the scaling factor in Figure 4(a), the photolysis yield was considerably lower in the visible probe experiments. This is consistent with calculated excitation yields (see § S2) and the larger sample thickness in the latter experiment, which is expected to enhance absorption effects. Therefore, the dynamics in the $\lambda_{probe} < 320$ nm range point to the decay of a single photo-induced species in 0.5 ps and 4 ps while the range $\lambda_{probe} > 320$ nm shows a 4 ps band splitting/broadening process, followed by band merging/narrowing in 16 ps, which is indicative of structural and symmetry changes. The appearance time of features assigned to $[Fe(CN)_5(H_2O)]^{3-}$ is ~16 ps, while the nature of the absorption bands present at the earliest times and their subsequent spectral evolution is discussed below.

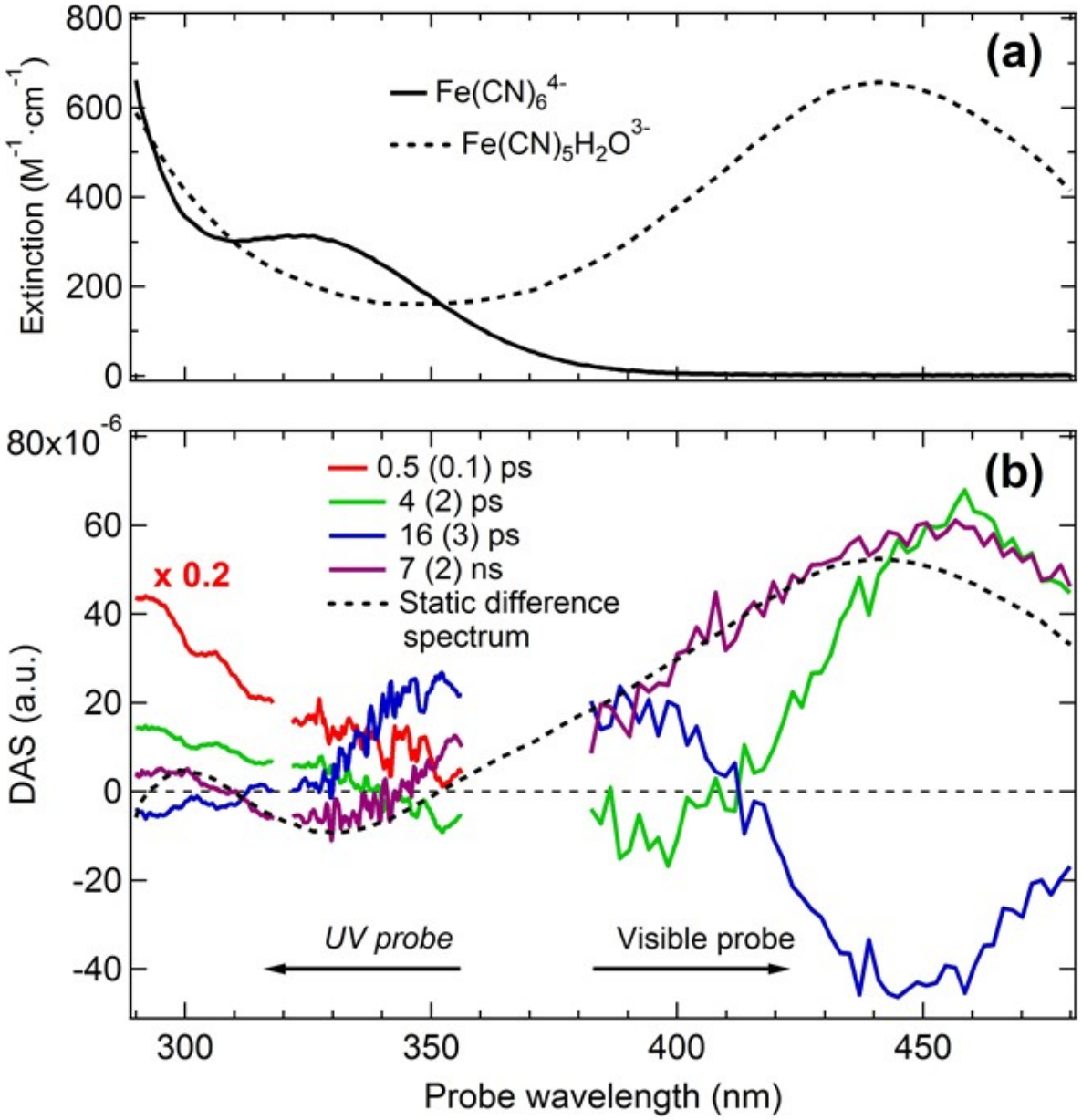

Figure 5. Combined decay associated spectra of aqueous $[Fe(CN)_6]^{4-}$. (a) Extinction coefficients of aqueous $[Fe(CN)_6]^{4-}$ (measured) and $[Fe(CN)_5(H_2O)]^{3-}$.[62,63] (b) Decay associated spectra from the 2D UV experiment (probe range ~280 - 350 nm) at 320 nm pump (x 0.1) and the white light probe experiment with 323 nm pump (probe range ~380 - 480 nm). The 0.5 ps component of the 2D UV data is additionally scaled (x 0.2). The static difference spectrum (black dashed line) corresponds to $\varepsilon_{323\,nm} = 0.1 \cdot \varepsilon_{320\,nm}$.

We have also estimated quantum yields as a function of excitation wavelength of the $[Fe(CN)_6]^{3-}$, e^-, and $[Fe(CN)_5(H_2O)]^{3-}$ photoproducts. As their extinction coefficients are known, the differences with respect to the $[Fe(CN)_6]^{4-}$ ground state extinction coefficient can be scaled to match the measured transient difference spectra, and quantum yields can be estimated from the resulting scaling factors. This procedure is described in detail in § S2. The extracted quantum yields for photoaquation (ϕ_{aq}) and photooxidation (ϕ_{ox}), along with those previously reported,[42,43] are shown in Fig. 6 and exhibit rather large uncertainties as they involve estimating the fraction of photoexcited molecules f_{exc}, for which we assumed an uncertainty of 100% to be conservative. However, the observed trends agree with the previously reported values.[42,43,47]

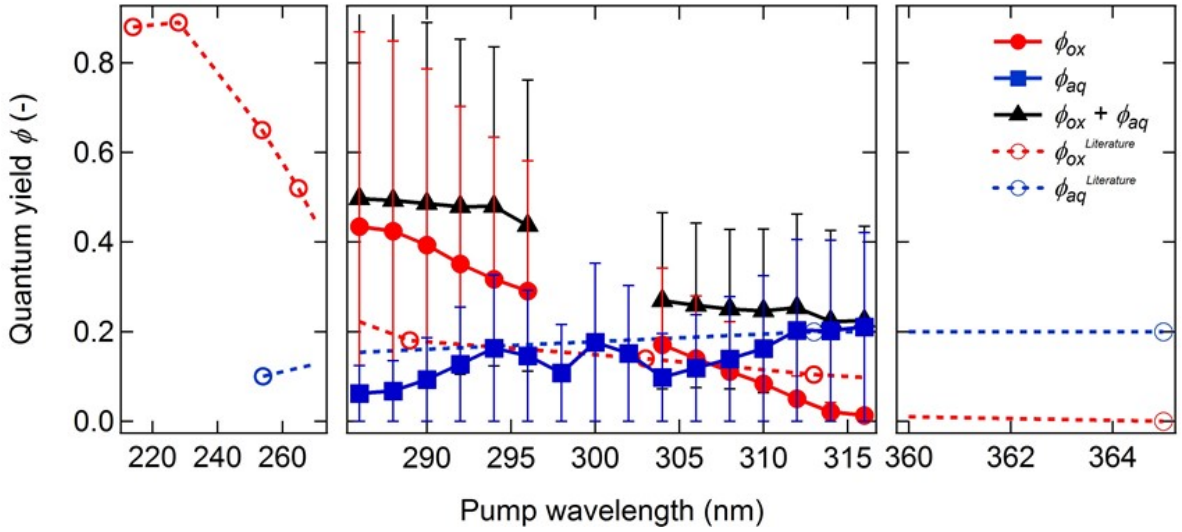

Figure 6. Quantum yields for the production of $[Fe(CN)_6]^{3-}$ (ϕ_{ox}, red filled circles) and $[Fe(CN)_5(H_2O)]^{3-}$ (ϕ_{aq}, blue filled squares), estimated from the ~7 ns DADAS (Figure S7(vii)) assuming no other contributing processes. ϕ_{ox} is taken as proportional to the action spectrum at λ_{probe} = 300 nm, where the photoaquation difference signal is approximately zero. For each λ_{pump} the static photooxidation spectrum scaled at λ_{probe} = 300 nm is subtracted from the respective 1D DAS and ϕ_{aq} is taken as proportional to the action spectrum of the resulting 2D dataset at λ_{probe} = 320 nm. Literature values for the quantum yields of the photooxidation[42] (at pH = 6.5) and photoaquation[43] (pH = 9) processes are shown as red and blue dashed lines respectively.

From Figure 6, we can draw the following conclusions: First, ϕ_{aq} shows no wavelength dependence between 360 nm and 310 nm, pointing to a Kasha-type behaviour for this photochemical channel, i.e. internal conversion processes lead to a relaxation to the lowest-energy state(s) that is (are) the doorway to the aquation reaction; Second, ϕ_{aq} decreases from ~20% to ~10% between 310 nm and 250 nm. This can be explained by the fact that ϕ_{ox} increases with increasing energy in this same range; Third, the total yield ($\phi_{aq} + \phi_{ox}$) also increases with increasing excitation energy, pointing to the increased photochemical decomposition via photooxidation with increasing excitation energy. Last, ($\phi_{aq} + \phi_{ox}$)<1 (typically ~0.5 at 285 nm and ~0.2 at 310 nm), suggesting that, either not all molecules are decomposed, or that a substantial part reform.

Although photoaquation is observed when we directly excite the lowest lying singlet state $^1T_{1g}$, the intermediate states leading to $[Fe(CN)_5(H_2O)]^{3-}$ remain unidentified. In order to complement the above analysis, we also carried out TRIR spectroscopy exciting at 320 nm, i.e. into the $^1T_{1g}$ state.

Figure 7 shows the TRIR transient spectra for $[Fe(CN)_6]^{4-}$ in H_2O. The corresponding kinetic traces are shown Figures S8 and additional transient spectra for H_2O are compared in Figure S9 with those for D_2O. The spectra appear similar for H_2O and D_2O, and they contain more spectral features than those obtained following 266 nm excitation. A very weak band due to $[Fe(CN)_6]^{3-}$ appears at 2117 cm^{-1} (inset in Figure 7). This is consistent with the 2D UV TA results (Figures 3(c), 5 and 6), which show a weak contribution of photoionization at 320 nm.

From the earliest times, Fig. 7 shows a depletion near the parent band at 2038 cm^{-1} along with a broad absorption band at *ca.* 2060 – 2090 cm^{-1}. The latter decays rapidly (τ_1 < 1 ps), concomitant with a partial recovery of the parent band (Figures S8(a) and (c)). The initial recovery corresponds to ~~about~~ ~40 % of the excited molecules and it can tentatively be assigned to geminate recombination of the CN^- radical with the pentacoordinated species formed by irradiation at 320 nm. The IR absorption bands of the aqueous cyanide ion have been reported at 2079 cm^{-1} with a bandwidth of 16-18 cm^{-1}.[65] Therefore, the 2060 – 2090 cm^{-1} band must contain other contributions, as will be seen later. Under 320 nm excitation, the TRIR spectrum obtained 2 ps after photolysis shows absorption bands near 2060 cm^{-1}

and ~2090 cm^{-1} (Figure 7). The 2060 cm^{-1} band is clearly distinguishable from the initial 2060-2090 cm^{-1} signal at early times as it grows in $\tau_2 = 4 \pm 2$ ps and decays in $\tau_3 = 23 \pm 4$ ps (Figure S8 (c)), giving rise to a new band at 2049 cm^{-1} that grows on a similar time scale (19 ± 4 ps, Figure S8(b)). It partially overlaps the parent bleach band. The 2049 cm^{-1} band is the IR band of the photoaquated species.[66] The parent bleach band exhibits an additional recovery in 23 ± 4 ps (Figure S8(a)). A similar behaviour is observed in D_2O.

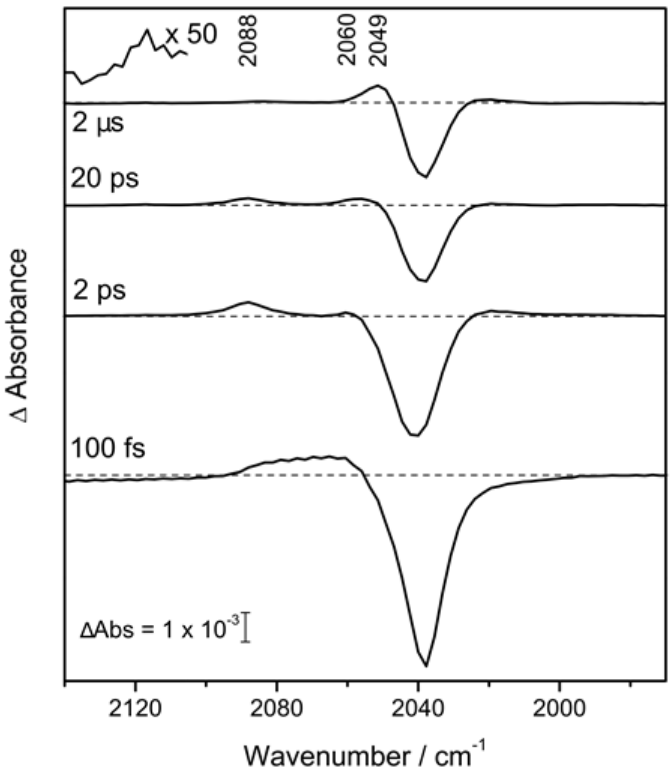

Figure 7. TRIR spectra of 18 mM $[Fe(CN)_6]^{4-}$ acquired in H_2O at several time-delays after photolysis at 320 nm. The inset shows the expanded region of the 2117 cm^{-1} ferricyanide stretch.

The assignment of the 2060 cm^{-1} and the ~2090 cm^{-1} bands is now discussed. Close inspection of the profile of the ~2090 cm^{-1} band shows that it is composed of more than one contribution (Figure S10): a) its width is significantly broader than the spectral resolution of the instrument (ca. 1.5 cm^{-1}); b) there

are clear shoulders on its high- and low-energy wings; c) the kinetic traces at the wings (Figures S8d and f) and at the maximum of the band (Figure S8e) confirm its composite nature. At 2088 cm^{-1} the intensity decays in $\tau_3 = 23 \pm 4$ ps, at 2090 cm^{-1} it grows in $\tau_2 = 4 \pm 2$ ps and decays in $\tau_3 = 23 \pm 4$ ps. At $\leq$ 2086 cm^{-1}, it first rapidly decays, likely due to overlap with the broad CN^- band at early times, and then undergoes a longer decay in 23 ± 4 ps. These various trends are further confirmed by the SVD analysis (§ S5) of the data set in H_2O, which provides the decay associated spectra (DAS) plotted in Figure 8. Four time components emerge from this analysis: i) The $\tau_1 = 0.5$ ps DAS reflects quite well the early time transient observed in Figures 7 and S8, with the bleach band at 2038 cm^{-1} having a long tail to the red, and the broad positive band in the 2055-2090 cm^{-1} range; ii) The $\tau_2 = 3.5$ ps DAS shows, along with the bleach band, weak positive features around 2020-2030 cm^{-1} and a negative one at ~2090 cm^{-1}. The long blue tail of the bleach may be a rising component of the band that appears at 2060 cm^{-1} in the 23 ps DAS and also contains a partial rise of the band characteristic for the aquated species (see below); iii) The $\tau_3 = 23$ ps DAS shows two new positive features at 2060 and ~2090 cm^{-1}. The distinction between the different bands making up the latter (Figure S10) is no longer as clear as seen in the time traces in Figure S8. However, all decay with τ_3, which is consistent with the corresponding DAS. Finally, the DAS at infinite time exhibits three positive features: weak ones around 2026 cm^{-1} and at 2088 cm^{-1} and a prominent one at ~2050 cm^{-1}. All three are characteristic of the aquated form as discussed below (Table 1).

Under 266 nm excitation, the ~2090 cm^{-1} band was significantly weaker and any subsequently formed species was not clear. However, spectral fitting of the parent bleach is consistent with formation of a band at 2049 cm^{-1}, which is formed at a similar rate to the decay of the ~2090 cm^{-1} species. Therefore, the TRIR results support photoaquation for both 266 and 320 nm excitation, but the quantum yield for the former is lower, consistent with the 2D-UV TA experiments. Most importantly, at both pump wavelengths, the various IR features exhibit kinetic behaviours that parallel those reported in the 2D UV and the visible TA spectra. Therefore in Table 1, we have grouped these bands according to their time scales, and we discuss their assignment below.

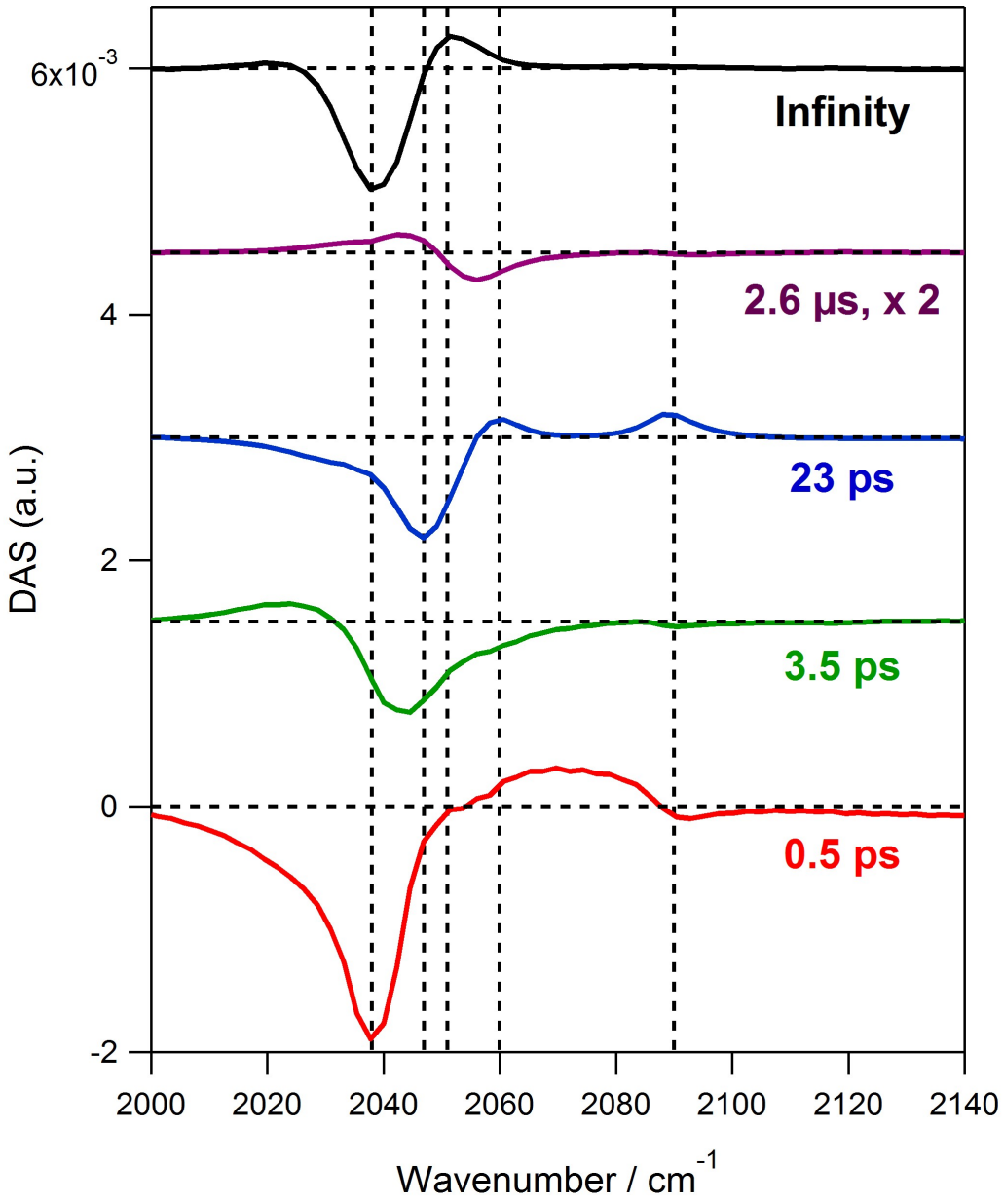
6x10-3
4
2
0
-2
DAS (a.u.)
Infinity
2.6 µs, x 2
23 ps
3.5 ps
0.5 ps
2000
2020
2040
2060
2080
2100
2120
2140
Wavenumber / cm-1

Figure 8. Top: transient spectra at different time delays. Bottom: Decay associated spectra (DAS) obtained from the singular value decomposition of the transient IR data sets in H_2O (τ_1= 0.5 ps, τ_2= 3.5 ps, τ_3= 23 ps, τ_4= infinity).

In order to aid the latter, we performed calculations of the electronic and vibrational energies using density functional theory (DFT, see § S6). We first calculate the ν_{CN} vibrational frequencies and structural parameters of the hexacoordinated complexes with an explicit unconstrained water solvent model (Figure S11), which is supported by previously published calculations of the spin-state energetics of $[Fe(H_2O)_6]^{3+}$ using a similar approach.[67] For the $[Fe(CN)_6]^{4-}$ complex in its ground state, the calculations give a frequency of 2040 cm^{-1} for the ν_{CN} band (Table S2), consistent with our experimental value of 2038 cm^{-1}. For the T_1 state of the complex, calculations predict bands at 2058, 2067 and 2079 cm^{-1}, with the first and last being the most intense ones. The calculated structure for this state in water shows a significant distortion: a large elongation (by about 20%) of the axial Fe-C bond (Table S3), found to be 2.40 Å compared to 1.92 Å in the ground state, while the equatorial bond lengths are 1.95 and 2.00 Å in the triplet state. The molecular orbitals (MOs) show that formation of the T_1 state involves the population of an antibonding dz^2-like orbital (Figures S12 and S13) and, consistent with the calculated axial elongation, this is expected to induce a Jahn-Teller distortion. The elongation of the axial Fe-C bonds is significantly larger than what was measured for Fe(II)-polypyridine complexes in their quintet states,[68] however, it is consistent with optimized triplet state calculations of Ru(II)-polypyridines.[please cite: Alary et al., Inorg. Chem. 47, (2008) 5259, doi: 10.1021/ic800246t] For example, two opposing Ru-N bonds of $[Ru(tap)]^{2+}$ (tap = 1-4-5-8-tetraazaphenanthrene) have been calculated to elongate from 2.104 Å in the ground state to 2.516 Å in the triplet ligand field state. Indeed, several computational studies on the photodissociation of Ru(II)-polypyridines have noted the dissociative nature of ^{3}LF states involving the population of orbitals with a high degree of σ-antibonding character between the axial CN ligands and the metal.[69,70] Our DFT calculations find the excitation energy for the lowest triplet state to be 2.86 eV, which is lower in energy than the predicted lowest quintet state (4.66 eV above the ground state), suggesting that it is less likely to be formed (Table S4).

Next, we consider the pentacoordinated complex: DFT geometry optimization and frequency calculations have been performed *in vacuo* and with a polarized continuum model (C-PCM) of the solvent for a range of possible pentacoordinated intermediates. The results are summarized in Table S5. The calculations with or without solvent predict a similar energy hierarchy of states: the triplet trigonal bipyramidal (^{3}TBP) structure being the lowest energy form, followed by the singlet square pyramidal (^{1}SP), and the triplet square pyramidal (^{3}SP). We note that the prediction of accurate singlet-triplet splittings is a challenging problem and can be sensitive to the nature of the exchange-correlation functional.[71] Calculations using the B3LYP* functional, which is parameterized with this in mind,[72] lead to a lowering of the singlet state energy, bringing the ^{1}SP structure within 2 kJ/mol of the ^{3}TBP configuration. Furthermore, the calculated C-PCM frequencies for the ^{3}TBP form shows two strong bands separated by over 20 cm^{-1}, consistent with the 23 ps-lived 2060 and 2090 cm^{-1} bands observed in the experiment, although the calculated frequencies are somewhat higher. The singlet spin square pyramidal structure has two bands split by less than 10 cm^{-1}.

Discussion

Assignment of bands:

We first identify the IR bands. Under 266 nm excitation and as stated above, the 2117 cm^{-1} band is due to the oxidised product $[Fe(CN)_6]^{3-}$, formed within the time-resolution of our experiments. This band partially decays on the timescale of tens of nanoseconds due to recombination with the photo-produced solvated electron (Figure S3(b)). Under 320 nm excitation, some of the formed IR features are also easily identifiable, such as: the $[Fe(CN)_6]^{3-}$ 2117 cm^{-1} band[46] and the photoaquated species $[Fe(CN)_5(H_2O)]^{3-}$ band at 2049 cm^{-1} (reported at 2043 ± 10 cm^{-1} in ref. [66], Table S2). In addition to the latter band, the DAS also revealed the weaker bands at ca. 2026 cm^{-1} and 2088 cm^{-1} that belong to the aquated species. The calculations indeed predict two weaker bands at 2037 and 2068 cm^{-1}, which we believe are associated to the former two (Table S2).

The broad < 1 ps IR band that appears in the 2060-2090 cm^{-1} region cannot be fully assigned to the CN^- ion (in a singlet X $^1\Sigma^+$ state, Table S2).[65] Since the $^3[Fe(CN)_6]^{4-}$ complex also absorbs in the same region according to the calculations (Table S2), we conclude that both $^3[Fe(CN)_6]^{4-}$ and CN^- species are observed within the time resolution of the experiment. This early-time IR absorption decays, concomitantly with the partial early time recovery of the parent. It is related to the $\tau_1 = 0.5$ ps process that appears in the UV (Figures 5 and S7) with maximum absorption < 280 nm, which we assign to the $[Fe(CN)_5]^{3-}$ fragment, as the CN^- fragment has no known bands in this region. The initial sub-ps decay of these IR and UV bands reflects the transient lifetime of the $^3[Fe(CN)_6]^{4-}$ state and the geminate recombination of $[Fe(CN)_5]^{3-}$ with CN^-. Just as for the IR, the UV and visible transitions belonging to $[Fe(CN)_6]^{4-}$, $[Fe(CN)_6]^{3-}$ and $[Fe(CN)_5(H_2O)]^{3-}$ are easily identifiable and Table 1 shows the assignments of all bands to the involved species and their lifetimes. Note that for the pentacoordinated complex, the predicted frequencies are higher than the experimental ones but lie within the expected level of accuracy for an open-shell transition metal complex, and given the approximate nature of the solvent model.

Mechanism of photoaquation:

From the body of ultrafast studies on electronically excited metal complexes,[73-75] electronic-vibrational relaxation proceeds at extremely fast time scales of a few tens of fs, to reach the lowest electronically excited state, in line with the Kasha rule. This also applies to chemical reactions. Indeed, the constant photoaquation yield for excitation wavelengths between 310 and 365 nm reflects this behaviour (the red most wavelength corresponds to the absorption threshold). It is therefore reasonable to assume that the relaxation cascade reaches the lowest triplet state prior to proceeding to dissociation. In addition, $\phi_{aq} + \phi_{ox} \leq 0.5$ down to 260 nm excitation (Figure 7), which implies that there is a substantial recovery of ground state $[Fe(CN)_6]^{4-}$ on an ultrafast time scale.

Photoexcitation at 320 nm into the $^1T_{1g}$ state is followed by Jahn-Teller distortion, due to the degeneracy of the excited state electronic configuration, and ISC into the lower triplet $^3T_{1g}$ states,

leading to dissociation of the molecule into $[Fe(CN)_5]^{3-}$ and CN^-. As explained above, the triplet state is characterized by the transfer of one electron from the bonding t_{2g} orbital to the antibonding e_g orbital (Figure S12), and a loosening of the Fe-CN bonds (Table S3), which may favor dissociation.

Therefore, given that from the earliest probed times in our experiments, we have formed an $[Fe(CN)_5]^{3-}$ species, the subsequent UV, visible and IR spectral changes reflect electronic/structural relaxation of this species. The CN^- ion is in a singlet state, and we assume that dissociation proceeds via a triplet state producing the nascent $[Fe(CN)_5]^{3-}$ in a triplet state, which can adopt either a trigonal bipyramidal (TBP) or a square pyramidal (SP) form. Furthermore, as described above (Table S5), the energies of the calculated states follow the order ^{3}TBP < ^{1}SP < ^{3}SP and the ^{3}SP form (52 kJ/mol higher than ^{3}TBP) is the most likely to be generated by dissociation and can undergo a further rearrangement process. τ_2 is reflected in a 3.5-4 ps rise of the bands at 2090 and 2060 cm^{-1} and the decay of the 2086 cm^{-1} band (Figure 8 and S8(d)) and corresponds to the production of ^{3}TBP. This process can either be associated to the ^{3}SP form undergoing a conformational change to the ^{3}TBP form, or a spin and conformational relaxation which would include a passage via the intermediate ^{1}SP form, where both SP species are predicted to exhibit two bands. The involvement of a singlet $[Fe(CN)_5]^{3-}$ moiety in the kinetic processes on the 4-20 ps timescale is very unlikely as similar singlet 16-electron intermediates have been shown to coordinate to very weakly coordinating solvents on the femtosecond timescale e.g. $Cr(CO)_5$ in alkane.[76] H_2O is a much more coordinating solvent to such fragments than alkanes and it is expected to react on faster timescales. This is further discussed below.

For the ^{3}TBP form, we have seen that the calculations predict two bands separated by ca. 20 cm^{-1} with an intensity ratio of ~3:1 between the lower and higher energy bands. This trend is reproduced between the 2060 cm^{-1} and ~2090 cm^{-1} bands, which in addition grow and decay on the same time scales (Figures S8(c) and S8(f)). This leads us to associate the 20-25 ps timescale of τ_3 to the decay of the ^{3}TBP complex. Because this is also the timescale for formation of the aquated species, we consider that formation of the latter proceeds from a ^{3}TBP precursor.

The rise-time (3.5-4 ps, τ_2) and decay (23 ps, τ_3) of the 2090 cm^{-1} and 2060 cm^{-1} bands are similar to those of the band in the 330 to 410 nm region and likewise, the decay time corresponds to the rise of the aquated complex. This, along with the fact that the 4 ps and 16 ps UV-visible bands are clearly correlated (Figure 5) suggests that we are still dealing with the $[Fe(CN)_5]^{3-}$ intermediate, consistent with the SP to TBP rearrangement.

Concomitant with the decay of the final $[Fe(CN)_5]^{3-}$ species, the aquated $[Fe(CN)_5(H_2O)]^{3-}$ (at 2049 cm^{-1} in the IR and *ca.* 440 nm in the UV) grows in ~23 ps. This is surprisingly slow for solvation of a 16-electron intermediate in a strongly coordinating solvent like water. For example, solvation by alkane solvents of $Cr(CO)_5$ formed by photoejection of CO from $Cr(CO)_6$ occurs in <1 ps.[76] Similar behaviour is observed for many metal carbonyl species in these weakly coordinating solvents.[16,77] Photolysis of $Fe(CO)_5$ in the condensed phase produces $^1Fe(CO)_4$,[13,26] which rapidly converts to $^3Fe(CO)_4$ before subsequent reaction with solvent species, which is very slow and strongly dependent on the nature of the solvent (ranging from 43 ps in EtOH[21] to 13 ns in heptane[23]). This scenario is very similar to the one proposed above where we are dealing with a triplet state species and the spin-change required to produce the final photoproduct decreases the rate of this process by two orders of magnitude compared to an unsaturated singlet metal carbonyl species.[26,76] The recovery of $[Fe(CN)_6]^{4-}$ occurs on all the above time constants: at the earliest times (< 1 ps), geminate recombination takes places concomitant with the disappearance of the broad IR absorption. This early recombination amounts to ~40 % of the initially bleached molecules. The 3-4 ps time constant of the parent bleach recovery reflects that already in the SP form some recombination to CN^- fragments is occurring. We consider this to be a geminate recombination, given its short time scale. Finally, further recombination occurs over ~20 ps, reaching ~25 % of the initially depleted molecules. This time scale is similar to that for photoaquation and therefore we conclude that the latter is the rate-determining step for the non-geminate recombination of $[Fe(CN)_5]^{3-}$ and CN^- species (there are more water molecules than CN^- fragments in the environment of the pentacoordinated species). The fact that no clear bands attributed

to CN appear at longer times may suggest that the broad IR absorption is predominantly due to $^3[Fe(CN)_6]^{4-}$ (Table S2).

Based on the above, we propose the following scenario for the photoaquation process, as summarized in Scheme 1: (i) Photoexcitation at 320 nm into the $^1T_{1g}$ state generates a triplet state of $[Fe(CN)_6]^{4-}$ within the time-resolution of our experiments. DFT predicts a lengthening of the Fe-C axial bonds in this state (Table S3); (ii) This favors or leads to dissociation of the molecule and leads to the appearance of the $[Fe(CN)_5]^{3-}$ fragment in the triplet SP form; (iii) Immediately after dissociation, partial geminate recombination of CN^- takes place with the SP $[Fe(CN)_5]^{3-}$ species (τ_1); (iv) the remaining pentacoordinated fragments undergo structural rearrangement the more stable ^{3}TBP form in 3-4 ps. We propose that at this stage, water molecules start to move in and compete with the remaining CN^- anions for bond formation (see Table 1 and Figure S8(b)) (τ_2); (v) The process of aquation (~20 ps, τ_2) is then slowed down by the spin change required to form the final product and due to steric constraints imposed by the TBP geometry of the intermediate and its reorganization.

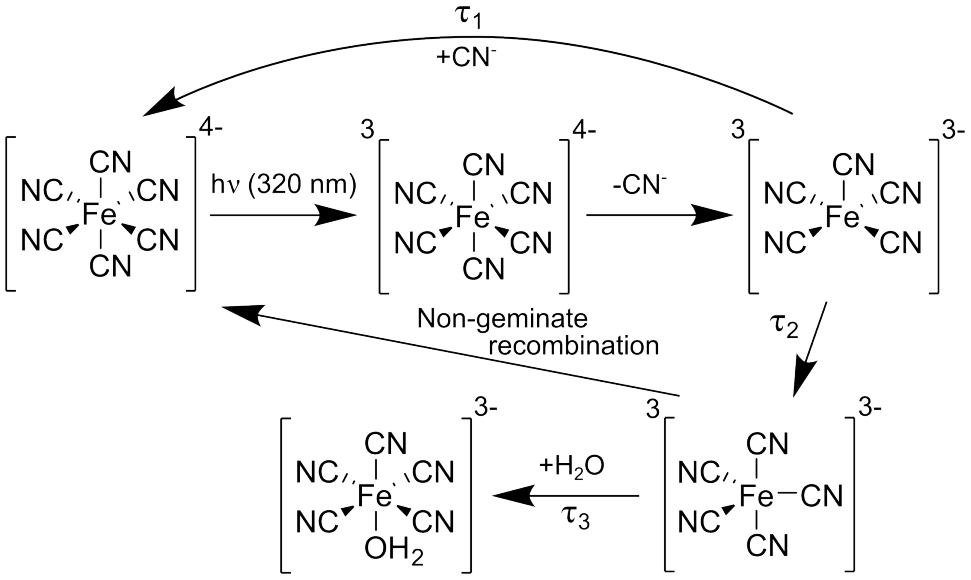

Scheme 1 : The proposed steps involved in the photoaquation of $[Fe(CN)_6]^{4-}$ after 320 nm absorption in H_2O.

While it seems intuitive that the system dissociates in a SP form, which does not impose steric constraints to the uptake of a water molecule, the binding of the latter by the TBP complex is less trivial as it supposes some rearrangement back to the square pyramidal form in order to accommodate the water molecule. Surely the participation of the water molecule is needed in order to make this rearrangement possible. Molecular dynamics simulations are needed to further elucidate the details of the water binding. This being said, the present observations invalidate the mechanism of dissociative interchange between $[Fe(CN)_6]^{4-}$ and H_2O proposed by Finston and Drickamer.[54]

Further evidence for the ~20 ps time scale process for binding of water being due to reaction with a triplet fragment comes from the fact that it is of the same order to magnitude as that reported for the case of $^3Fe(CO)_5$ in methanol,[20,21] and faster than the corresponding reaction in *n*-heptane, in supercritical xenon and supercritical CH_4,[23] but it is notably different to the cases of singlet reactivity of $Fe(CO)_5$ in ethanol[26] and $[Cr(CO)_4(bpy)]$ in methanol.[28,30] The latter two cases are remarkable in that solvent binding occurs in a few 100s fs, i.e. time scales typical of dissociation, while the solvent molecules are at thermal energies. As mentioned in the introduction, the very short time scale ($\leq$ 300 fs) for solvent substitution in the case of $Fe(CO)_5$ in ethanol[26] was justified by the existence of an interaction between the solvent molecules and the mother solute based on IR studies and DFT calculations.[78] It should also be noted that this process pertains only to $^1Fe(CO)_4$, while $^3Fe(CO)_4$ was found to persist until the end of the experiment, consistent with the much slower rate of solvation found earlier and relevant to our experiments where solvation occurs on a relatively slow timescale because of the required spin and conformational changes. Recent *ab initio* Car-Parrinello molecular dynamics simulations have so far not supported the ultrafast binding of a solvent molecule in $Fe(CO)_5$.[27] In the present case, despite indications from 2D IR[40,55] and x-ray studies[39,41] of a specific interaction of $[Fe(CN)_6]^{4-}$ with water molecules, the solvent does not seem to play an essential role in the photochemistry of the molecule, except to allow the process of geminate recombination by caging the fragments within the first ps. The lack of an isotope effect on the kinetics of photoaquation is also in

line with the relatively long time scales of the reported processes which is governed by barrier for conversion of $^3[Fe(CN)_5]^{3-}$ to $^1[Fe(CN)_5(H_2O)]^{3-}$.

Other examples of photoaquation reactions of metal cyanides include $[Co(CN)_6]^{3-}$, which presents an interesting target of investigation as it is isoelectronic to $[Fe(CN)_6]^{4-}$. $[Co(CN)_6]^{3-}$ has not been the subject of any ultrafast time-resolved investigations but early studies based on ligand exchange reactions[36] and pressure-dependent quantum yield measurements[79] have pointed toward a dissociative interchange mechanism in the formation of $[Co(CN)_5(H_2O)]^{2-}$. This difference to the ferrocyanide case may be indicative of an increased dissociation energy of the Co-CN bond.

Finally, the increased photoionization yield with increasing energy points to a non-Kasha behaviour for this channel, which is logical since electron dynamics are much faster than the nuclear dynamics associated with intramolecular relaxation. This is also reflected in the decrease of the photoaquation quantum yield upon excitation of the CTTS states and consistent with the lack of an ultrafast CTTS fluorescence, which we could not detect.[48]

The body of work on ultrafast intramolecular relaxation of complex molecular systems in solution show that the Kasha Rule is largely verified and exceptions are rare.[75,80] Intramolecular energy redistribution occurs at extremely short time scales, reaching even values shorter than the high frequency vibrational time scales,[73,81] while intersystem crossing events also occur at very short time scales.[74] It is therefore expected that the Kasha Rule will also be verified for photochemical reactions, i.e. the significant chemistry involves only the lowest states. The only reaction channel that competes in any significant way with intramolecular energy redistribution are photooxidation events, as the release of an electron must occur at significantly shorter time scales than the vibrational ones. This is valid for CTTS dynamics, as in the present case, or even interfacial electron injection of a molecular adsorbate on a semiconductor substrate.[82-85]

Conclusions

We have carried out a detailed investigation of the excitation energy-dependent ultrafast photochemistry of aqueous $[Fe(CN)_6]^{4-}$. Combining advanced ultrafast spectroscopic tools: 2-dimensional UV spectroscopy, visible and infrared transient absorption spectroscopy, along with quantum chemical calculations, we have elucidated the photoaquation mechanism of $[Fe(CN)_6]^{4-}$ in water. The initial events are an ultrafast intramolecular relaxation to the lowest triplet state and dissociation of the molecule with release of a CN^- fragment. Part of the fragments recombine geminately within the solvent cage. All these events (intramolecular energy redistribution, dissociation, geminate recombination) occur in <0.5 ps. The subsequent observed dynamics is all due to the $[Fe(CN)_5]^{3-}$ fragment, which is initially formed in the square pyramidal configuration in the triplet state. It then undergoes conformational changes in 3-4 ps to the lower lying triplet state of the trigonal pyramidal form. Binding of water molecules takes place in ~20 ps and shows no isotope effect. This relatively long time scale must reflect a rearrangement of the pentacoordinated trigonal bipyramidal complex to a geometry favoring uptake of a water molecule. Molecular dynamics simulations will be needed to further support this scenario. In addition, ultrafast x-ray spectroscopy provides ideal tools to detect both the nuclear, electronic and spin structure of the intermediate pentacoordinated form[86] and studies are on-going at x-ray free electron lasers to this purpose.

Acknowledgements:

This work was funded by the Swiss NSF via contracts 124520,135502 and 158890 and via the NCCR MUST. We also thank the University of Nottingham and EPSRC for funding.

Table 1. IR, UV and visible bands and their kinetics upon 320 nm excitation

Vibrational bands in H_2O (D_2O)	Electronic bands in H_2O	Assignment

Frequency cm^{-1}	τ_{rise} (ps)	τ_{decay} (ps)	Wavelength range (nm)	τ_{rise} (ps)	τ_{decay} (ps)	
2038 (bleach)	<0.5 (<0.5)≈$\tau_{IRF,IR}$	τ_1<1 (<1), τ_2=4±2 (3±1), τ_3=23±4 (24±5), stable	280-320 (bleach)	<0.15=$\tau_{IRF,UV}$	τ_3=16±3, stable	$[Fe(CN)_6]^{4-}$
2050-2090	<0.5 (<0.5) ≈ $\tau_{IRF,IR}$	τ_1< 1 (<1)				CN^- radical in the IR
2086	<1 (<1)	26±4[a], (22±4)[a]	280-340 410-470	<0.15= $\tau_{IRF,UV}$ <0.7= $\tau_{IRF,Vis}$	τ_1=0.5, τ_2=4±2 τ_1<0.7= $\tau_{IRF,Vis}$ τ_2=4±2	$[Fe(CN)_5]^{3-}$ SP
2090 2060	τ_2=4±2 (3±2) τ_2=4±2 (3±2)	τ_3=23±4 (22±4) τ_3=23±4 (19±7)	340-410	τ_2=4±2	τ_3=16±3	$[Fe(CN)_5]^{3-}$ TBP
2026[b], 2049, 2088	τ_3=19±4[c], (23±5)	stable	350-470 Max. at 450	τ_3=16±3	τ_4>7200	$[Fe(CN)_5(H_2O)]^{3-}$
2117	<0.5≈ $\tau_{IRF,IR}$	stable	Broad UV-Vis spectrum	<0.15= $\tau_{IRF,UV}$	τ_4>7200	$[Fe(CN)_6]^{3-}$

[a]An additional <1 ps contribution is observed, which can be attributed to overlap with the CN^- band (see Figures 7 and S8). [b]It is difficult to resolve the experimental band at 2026 cm^{-1} due to overlap with the parent bleach. The assignment is done on the basis of band-fitting, DFT calculations (Table S2) and previous work.[66] [c]An additional 4 ps transient is observed.

References

(1) Franck, J.; Rabinowitsch, E. *Transactions of the Faraday Society* **1934**, *30*, 120.
(2) Voth, G. A.; Hochstrasser, R. M. *J Phys Chem-Us* **1996**, *100*, 13034.
(3) Carpenter, B. K.; Harvey, J. N.; Orr-Ewing, A. J. *J Am Chem Soc* **2016**, *138*, 4695.
(4) Schwentner, N.; Bressler, C.; Lawrence, W.; Xu, J.; Chergui, M. *Chem Phys* **1994**, *189*, 205.
(5) Schriever, R.; Chergui, M.; Kunz, H.; Stepanenko, V.; Schwentner, N. *J Chem Phys* **1989**, *91*, 4128.
(6) Apkarian, V. A.; Schwentner, N. *Chem Rev* **1999**, *99*, 1481.
(7) Harris, A. L.; Brown, J. K.; Harris, C. B. *Annu Rev Phys Chem* **1988**, *39*, 341.
(8) Fleming, G. R.; vanGrondelle, R. *Curr Opin Struc Biol* **1997**, *7*, 738.
(9) Schriever, R.; Chergui, M.; Unal, O.; Schwentner, N.; Stepanenko, V. *J Chem Phys* **1990**, *93*, 3245.
(10) Erras-Hanauer, H.; Clark, T.; van Eldik, R. *Coordin Chem Rev* **2003**, *238*, 233.
(11) Rotzinger, F. P. *Chem Rev* **2005**, *105*, 2003.
(12) Swart, M.; Costas Salgueiro, M. *Spin states in biochemistry and inorganic chemistry : influence on structure and reactivity*; John Wiley & Sons, 2015.
(13) Poliakoff, M.; Turner, J. J. *Angew Chem Int Edit* **2001**, *40*, 2809.
(14) Simon, J. D.; Xie, X. L. *J Phys Chem-Us* **1986**, *90*, 6751.
(15) Joly, A. G.; Nelson, K. A. *J Phys Chem-Us* **1989**, *93*, 2876.
(16) Joly, A. G.; Nelson, K. A. *Chem Phys* **1991**, *152*, 69.
(17) Simon, J. D.; Xie, X. L. *J Phys Chem-Us* **1989**, *93*, 291.
(18) Xie, X. L.; Simon, J. D. *J Am Chem Soc* **1990**, *112*, 1130.
(19) Kotz, K. T.; Yang, H.; Snee, P. T.; Payne, C. K.; Harris, C. B. *J Organomet Chem* **2000**, *596*, 183.
(20) Snee, P. T.; Payne, C. K.; Kotz, K. T.; Yang, H.; Harris, C. B. *J Am Chem Soc* **2001**, *123*, 2255.
(21) Snee, P. T.; Payne, C. K.; Mebane, S. D.; Kotz, K. T.; Harris, C. B. *J Am Chem Soc* **2001**, *123*, 6909.
(22) Yang, H.; Snee, P. T.; Kotz, K. T.; Payne, C. K.; Harris, C. B. *J Am Chem Soc* **2001**, *123*, 4204.
(23) Portius, P.; Yang, J. X.; Sun, X. Z.; Grills, D. C.; Matousek, P.; Parker, A. W.; Towrie, M.; George, M. W. *J Am Chem Soc* **2004**, *126*, 10713.
(24) Besora, M.; Carreon-Macedo, J. L.; Cowan, A. J.; George, M. W.; Harvey, J. N.; Portius, P.; Ronayne, K. L.; Sun, X. Z.; Towrie, M. *J Am Chem Soc* **2009**, *131*, 3583.
(25) Ahr, B.; Chollet, M.; Adams, B.; Lunny, E. M.; Laperle, C. M.; Rose-Petruck, C. *Phys Chem Chem Phys* **2011**, *13*, 5590.

(26) Wernet, P.; Kunnus, K.; Josefsson, I.; Rajkovic, I.; Quevedo, W.; Beye, M.; Schreck, S.; Grubel, S.; Scholz, M.; Nordlund, D.; Zhang, W.; Hartsock, R. W.; Schlotter, W. F.; Turner, J. J.; Kennedy, B.; Hennies, F.; de Groot, F. M. F.; Gaffney, K. J.; Techert, S.; Odelius, M.; Fohlisch, A. *Nature* **2015**, *520*, 78.

(27) Kunnus, K.; Josefsson, I.; Rajkovic, I.; Schreck, S.; Quevedo, W.; Beye, M.; Weniger, C.; Grübel, S.; Scholz, M.; Nordlund, D.; Zhang, W.; Hartsock, R. W.; Gaffney, K. J.; Schlotter, W. F.; Turner, J. J.; Kennedy, B.; Hennies, F.; de Groot, F. M. F.; Techert, S.; Odelius, M.; Wernet, P.; Föhlisch, A. *Structural Dynamics* **2016**, *3*, 043204.

(28) Farrell, I. R.; Matousek, P.; Towrie, M.; Parker, A. W.; Grills, D. C.; George, M. W.; Vlcek, A. *Inorg Chem* **2002**, *41*, 4318.

(29) Vichova, J.; Hartl, F.; Vlcek, A. *J Am Chem Soc* **1992**, *114*, 10903.

(30) Farrell, I. R.; Matousek, P.; Vlcek, A. *J Am Chem Soc* **1999**, *121*, 5296.

(31) Farrell, I. R.; Matousek, P.; Kleverlaan, C. J.; Vlcek, A. *Chem-Eur J* **2000**, *6*, 1386.

(32) Farrell, I. R.; Vlcek, A. *Coordin Chem Rev* **2000**, *208*, 87.

(33) Tfouni, E.; Krieger, M.; McGarvey, B. R.; Franco, D. W. *Coordin Chem Rev* **2003**, *236*, 57.

(34) Liu, Y.; Turner, D. B.; Singh, T. N.; Angeles-Boza, A. M.; Chouai, A.; Dunbar, K. R.; Turro, C. *J Am Chem Soc* **2009**, *131*, 26.

(35) Asperger, S. *Transactions of the Faraday Society* **1952**, *48*, 617.

(36) Wrighton, M.; Hammond, G. S.; Gray, H. B. *J Am Chem Soc* **1971**, *93*, 5254.

(37) MacDiarmid, A. G.; Hall, N. F. *J Am Chem Soc* **1953**, *75*, 5204.

(38) MacDiarmid, A. G.; Hall, N. F. *J Am Chem Soc* **1954**, *76*, 4222.

(39) Aziz, E. F.; Rittmann-Frank, M. H.; Lange, K. M.; Bonhommeau, S.; Chergui, M. *Nat Chem* **2010**, *2*, 853.

(40) Prampolini, G.; Yu, P. Y.; Pizzanelli, S.; Cacelli, I.; Yang, F.; Zhao, J. A.; Wang, J. P. *J Phys Chem B* **2014**, *118*, 14899.

(41) Penfold, T. J.; Reinhard, M.; Rittmann-Frank, M. H.; Tavernelli, I.; Rothlisberger, U.; Milne, C. J.; Glatzel, P.; Chergui, M. *J Phys Chem A* **2014**, *118*, 9411.

(42) Shirom, M.; Stein, G. *J Chem Phys* **1971**, *55*, 3372.

(43) Shirom, M.; Stein, G. *J Chem Phys* **1971**, *55*, 3379.

(44) Mialocq, J. C.; Sutton, J.; Goujon, P. *Nuovo Cimento B* **1981**, *63*, 317.

(45) Pommeret, S.; Naskrecki, R.; van der Meulen, P.; Menard, M.; Vigneron, G.; Gustavsson, T. *Chemical Physics Letters* **1998**, *288*, 833.

(46) Anderson, N. A.; Hang, K.; Asbury, J. B.; Lian, T. Q. *Chemical Physics Letters* **2000**, *329*, 386.

(47) Lenchenkov, V.; Kloepfer, J.; Vilchiz, V.; Bradforth, S. E. *Chemical Physics Letters* **2001**, *342*, 277.

(48) Reinhard, M.; Penfold, T. J.; Lima, F. A.; Rittmann, J.; Rittmann-Frank, M. H.; Abela, R.; Tavernelli, I.; Rothlisberger, U.; Milne, C. J.; Chergui, M. *Structural Dynamics* **2014**, *1*, 024901.

(49) Messina, F.; Bram, O.; Cannizzo, A.; Chergui, M. *Nature Communications* **2013**, *4*, 2119.

(50) Gray, H. B.; Beach, N. A. *J Am Chem Soc* **1963**, *85*, 2922.

(51) Toma, H. E.; Batista, A. A.; Gray, H. B. *J Am Chem Soc* **1982**, *104*, 7509.

(52) Gaspar, V.; Beck, M. T. *Polyhedron* **1983**, *2*, 387.

(53) Bolvin, H. *J Phys Chem A* **1998**, *102*, 7525.

(54) Finston, M. I.; Drickamer, H. G. *J Phys Chem-Us* **1981**, *85*, 50.

(55) Yu, P. Y.; Yang, F.; Zhao, J.; Wang, J. P. *J Phys Chem B* **2014**, *118*, 3104.

(56) Aubock, G.; Consani, C.; Monni, R.; Cannizzo, A.; van Mourik, F.; Chergui, M. *Rev Sci Instrum* **2012**, *83*.

(57) Aubock, G.; Consani, C.; van Mourik, F.; Chergui, M. *Opt Lett* **2012**, *37*, 2337.

(58) Consani, C.; Aubock, G.; van Mourik, F.; Chergui, M. *Science* **2013**, *339*, 1586.

(59) Greetham, G. M.; Burgos, P.; Cao, Q. A.; Clark, I. P.; Codd, P. S.; Farrow, R. C.; George, M. W.; Kogimtzis, M.; Matousek, P.; Parker, A. W.; Pollard, M. R.; Robinson, D. A.; Xin, Z. J.; Towrie, M. *Appl Spectrosc* **2010**, *64*, 1311.

(60) Greetham, G. M.; Donaldson, P. M.; Nation, C.; Sazanovich, I. V.; Clark, I. P.; Shaw, D. J.; Parker, A. W.; Towrie, M. *Appl Spectrosc* **2016**, *70*, 645.

(61) Chen, X. Y.; Larsen, D. S.; Bradforth, S. E.; van Stokkum, I. H. M. *J Phys Chem A* **2011**, *115*, 3807.

(62) Gale, R.; Mccaffer.Aj *J Chem Soc Dalton* **1973**, 1344.

(63) Montenegro, A. C.; Dabrowski, S. G.; Gutierrez, M. M.; Amorebieta, V. T.; Bari, S. E.; Olabe, J. A. *Inorg Chim Acta* **2011**, *374*, 447.

(64) Helbing, J.; Bonacina, L.; Pietri, R.; Bredenbeck, J.; Hamm, P.; van Mourik, F.; Chaussard, F.; Gonzalez-Gonzalez, A.; Chergui, M.; Ramos-Alvarez, C.; Ruiz, C.; Lopez-Garriga, J. *Biophysical Journal* **2004**, *87*, 1881.

(65) Hamm, P.; Lim, M.; Hochstrasser, R. M. *The Journal of chemical physics* **1997**, *107*, 10523.

(66) Herington, E. F. G.; Kynaston, W. *J Chem Soc* **1955**, 3555.

(67) Radon, M.; Gassowska, K.; Szklarzewicz, J.; Broclawik, E. *Journal of chemical theory and computation* **2016**, *12*, 1592.

(68) Gawelda, W.; Pham, V. T.; Benfatto, M.; Zaushitsyn, Y.; Kaiser, M.; Grolimund, D.; Johnson, S. L.; Abela, R.; Hauser, A.; Bressler, C.; Chergui, M. *Phys Rev Lett* **2007**, *98*, 057401.

(69) Salassa, L.; Garino, C.; Salassa, G.; Gobetto, R.; Nervi, C. *J Am Chem Soc* **2008**, *130*, 9590.

(70) Tu, Y.-J.; Mazumder, S.; Endicott, J. F.; Turro, C.; Kodanko, J. J.; Schlegel, H. B. *Inorg Chem* **2015**, *54*, 8003.

(71) Delcey, M. G.; Freitag, L.; Pedersen, T. B.; Aquilante, F.; Lindh, R.; Gonzalez, L. *J Chem Phys* **2014**, *140*.
(72) Reiher, M.; Salomon, O.; Hess, B. A. *Theor Chem Acc* **2001**, *107*, 48.
(73) Bräm, O.; Messina, F.; El-Zohry, A.; Cannizzo, A.; Chergui, M. *Chem Phys* **2012**, *393*, 51.
(74) Aubock, G.; Chergui, M. *Nat Chem* **2015**, *7*, 629.
(75) Chergui, M. *Accounts Chem Res* **2015**, *48*, 801.
(76) Simon, J. D.; Xie, X. *J Phys Chem-Us* **1987**, *91*, 5538.
(77) Dougherty, T.; Heilweil, E. J. *Chemical physics letters* **1994**, *227*, 19.
(78) Lee, T.; Benesch, F.; Jiang, Y.; Rose-Petruck, C. G. *Chem Phys* **2004**, *299*, 233.
(79) Angermann, K.; van Eldik, R.; Kelm, H.; Wasgestian, F. *Inorg Chim Acta* **1981**, *49*, 247.
(80) Chergui, M. *Dalton T* **2012**, *41*, 13022.
(81) Messina, F.; Pomarico, E.; Silatani, M.; Baranoff, E.; Chergui, M. *The Journal of Physical Chemistry Letters* **2015**, 4475.
(82) Huber, R.; Moser, J. E.; Gratzel, M.; Wachtveitl, J. *J Phys Chem B* **2002**, *106*, 6494.
(83) Schnadt, J.; Bruhwiler, P. A.; Patthey, L.; O'Shea, J. N.; Sodergren, S.; Odelius, M.; Ahuja, R.; Karis, O.; Bassler, M.; Persson, P.; Siegbahn, H.; Lunell, S.; Martensson, N. *Nature* **2002**, *418*, 620.
(84) Bram, O.; Cannizzo, A.; Chergui, M. *Phys Chem Chem Phys* **2012**, *14*, 7934.
(85) Huber, R.; Dworak, L.; Moser, J. E.; Grätzel, M.; Wachtveitl, J. *The Journal of Physical Chemistry C* **2016**, *120*, 8534.
(86) Milne, C. J.; Penfold, T. J.; Chergui, M. *Coordin Chem Rev* **2014**, *277–278*, 44.